

RESEARCH ARTICLE

10.1002/2016MS000731

Cloud-edge mixing: Direct numerical simulation and observations in Indian Monsoon clouds

Bipin Kumar¹, Sudarsan Bera² , Thara V. Prabha² , and Wojceich W. Grabowski³ 

Key Points:

- Idealized DNS simulations show mixing characteristics and droplet size distributions similar to airborne observations of natural convective clouds
- Simulated evaporation of cloud droplets near cloud edges drives larger-scale buoyancy driven coherent structures
- Similarity between mixing diagrams in DNS and observations questions use of such diagrams in developing heuristic arguments from observational data

Correspondence to:

B. Kumar,
bipink@tropmet.res.in

Citation:

Kumar, B., S. Bera, T. V. Prabha, and W. W. Grabowski (2017), Cloud-edge mixing: Direct numerical simulation and observations in Indian Monsoon clouds, *J. Adv. Model. Earth Syst.*, 9, 332–353, doi:10.1002/2016MS000731.

Received 10 JUN 2016

Accepted 5 JAN 2017

Accepted article online 10 JAN 2017

Published online 1 FEB 2017

¹High Performance Computing Systems, Indian Institute of Tropical Meteorology, Pune, India, ²Physics and Dynamics of Tropical Cloud, Indian Institute of Tropical Meteorology, Pune, India, ³Mesoscale and Microscale Meteorology Laboratory, National Center for Atmospheric Research, Boulder, Colorado, USA

Abstract A direct numerical simulation (DNS) with the decaying turbulence setup has been carried out to study cloud-edge mixing and its impact on the droplet size distribution (DSD) applying thermodynamic conditions observed in monsoon convective clouds over Indian subcontinent during the Cloud Aerosol Interaction and Precipitation Enhancement EXperiment (CAIPEEX). Evaporation at the cloud-edges initiates mixing at small scale and gradually introduces larger-scale fluctuations of the temperature, moisture, and vertical velocity due to droplet evaporation. Our focus is on early evolution of simulated fields that show intriguing similarities to the CAIPEEX cloud observations. A strong dilution at the cloud edge, accompanied by significant spatial variations of the droplet concentration, mean radius, and spectral width, are found in both the DNS and in observations. In DNS, fluctuations of the mean radius and spectral width come from the impact of small-scale turbulence on the motion and evaporation of inertial droplets. These fluctuations decrease with the increase of the volume over which DNS data are averaged, as one might expect. In cloud observations, these fluctuations also come from other processes, such as entrainment/mixing below the observation level, secondary CCN activation, or variations of CCN activation at the cloud base. Despite large differences in the spatial and temporal scales, the mixing diagram often used in entrainment/mixing studies with aircraft data is remarkably similar for both DNS and cloud observations. We argue that the similarity questions applicability of heuristic ideas based on mixing between two air parcels (that the mixing diagram is designed to properly represent) to the evolution of microphysical properties during turbulent mixing between a cloud and its environment.

1. Introduction

One of the fundamental problems in cloud physics is the impact of entrainment on the cloud droplet size distribution (DSD) in warm (ice-free) convective clouds [e.g., Lasher-Trapp et al., 2005; Devenish et al., 2012; Kumar et al., 2012, 2013, 2014, and references therein]. The amount of evaporation that is needed as a result of entrainment is controlled by the bulk thermodynamics, but this does not allow predicting the modification of the DSD. In a nutshell, required evaporation can be accomplished by either a uniform evaporation of all droplets (as in the homogeneous mixing), or by a complete evaporation of some droplets leaving the rest unchanged (as in the extremely inhomogeneous mixing), or by a combination of the two [e.g., Baker and Latham, 1979; Baker et al., 1980; Jensen and Baker, 1989; Burnet and Brenguier, 2007; Andrejczuk et al., 2009; Lehman et al., 2009; Jarecka et al., 2013b; Tölle and Krueger, 2014; Bera et al., 2016b].

The mixing characteristics have been argued to depend on the relative magnitudes of the mixing time scale (that is based on the relevant spatial scale and the turbulence intensity) and on the phase change (droplet evaporation) time scale [Baker et al., 1984; Burnet and Brenguier, 2007; Kumar et al., 2012, among others]. Consequences of the turbulent entrainment are observed from the cloud core to cloud edges with dynamic and thermodynamic processes covering a broad range of spatial and temporal scales. The spatial range covers scales from the size of an entraining eddy (not much smaller than the convective cloud itself) down to the Kolmogorov microscale, around 1 mm in atmospheric turbulence. Due to the range of spatial scales, the mixing time scale can vary broadly and this makes prediction of the mixing characteristics difficult. The multiscale entrainment and associated dynamics creates a complex cloud-clear air interface across which molecular transport and droplet sedimentation lead to the eventual homogenization of initially coarsely mixed volume [e.g., Grabowski, 1993; Andrejczuk et al., 2004, 2006, 2009; Kumar et al., 2012, 2013, 2014, hereafter KSS14]. As a result, the DSD can vary significantly after the mixture is homogenized and can impact

© 2017. The Authors.

This is an open access article under the terms of the Creative Commons Attribution-NonCommercial-NoDerivs License, which permits use and distribution in any medium, provided the original work is properly cited, the use is non-commercial and no modifications or adaptations are made.

such key cloud field properties as the cloud albedo [e.g., *Brenguier et al.*, 2000] or propensity to produce precipitation through collision/coalescence [e.g., *Telford and Chai*, 1980; *Cooper*, 1989; *Cooper et al.*, 2013].

Monsoon deep cumulus clouds over Indian subcontinent are essential for the surface rainfall. It follows that understanding dynamical and microphysical processes controlling rain formation within those clouds is of critical concern. Cloud Aerosol Interaction and Precipitation Enhancement Experiment (CAIPEEX) over Indian subcontinent has brought out unique features of raindrop formation mechanism in monsoon clouds [e.g., *Prabha et al.*, 2011, 2012; *Bera et al.*, 2016a]. One of the most important factors for the monsoon prediction is a better representation of cloud processes. These representations can be improved by carrying out small-scale simulations (such as Large Eddy Simulation, LES, or Direct Numerical Simulation, DNS [e.g., *Kumar et al.*, 2012, 2013; *Jarecka et al.*, 2013a; *Hoffman et al.*, 2014, and references therein]; or dedicated high-resolution field observations [e.g., *Gerber et al.*, 2008; *Yum et al.*, 2015]. Observations are often used to design and validate model simulations [e.g., *Stevens et al.*, 2005; *VanZanten et al.*, 2011], but simulated and observed DSDs are seldom compared in detail. *Khain et al.* [2013] compare CAIPEEX observations with 2-D and 3-D LES simulation results and show that first raindrops form in undiluted cores with high liquid water content. This paper makes an attempt to compare DNS simulated evolution of the DSD with aircraft observations.

We use observations of cumulus clouds from CAIPEEX over India [*Prabha et al.*, 2011, 2012; *Bera et al.*, 2016a] to initialize highly idealized DNS simulations in which a small cloudy volume with an undiluted polydisperse DSD from observations is allowed to mix with a cloud-free ambient air. The main focus is on cloud-edge mixing and its effect on the DSD. The key advantage of DNS is that it simulates relevant processes from the first principles, perhaps with the exception of the details of the cloud droplet condensational and evaporation. The latter requires resolving temperature and water vapor gradients near the droplet, that is, at spatial scales of a few microns. Because of the small mass loading and thus large mean distance between the droplets (compared to the droplet radius) an approach based on macroscopic droplet growth equations applied at the cloud microscale is sufficient [see Appendix in *Valliancourt et al.*, 2001]. DNS faithfully represents fine-scale processes modifying DSD albeit at a relatively narrow range of spatial scales close to the Kolmogorov microscale. In situ cloud observations, on the other hand, provide data at scales not far from the scale of entraining eddies (down to a few meters), especially for the cloud dynamics. This is because of the combined effect of a limited spatial resolution (due to the aircraft cruising speed) and the response time of aircraft-mounted instruments. Thus, it can be argued that direct comparisons between DNS and cloud observations are impossible. This paper challenges this view by comparing DNS predicted droplet characteristics to in situ aircraft observations.

The paper is organized as follows. The next section presents the DNS model and details the setup of model simulations. Section 3 discusses model results focusing on the DSD change originating from the mixing between a cloud and cloud-free subsaturated air. Section 4 presents aircraft observations in the same format as some of the DNS results and documents interesting similarities between DNS and aircraft observations. Discussion in section 5 concludes the paper.

2. DNS Model and Model Setup

The DNS numerical model is the same as in KSS14. Details of the model equations are provided in Appendix A. The Eulerian fluid flow model solves incompressible viscous Navier-Stokes equations supplemented by the conservation equations for the temperature and water vapor mixing ratio that include sources and sinks due to diffusional growth of cloud droplets (cf. equations (2)–(5) in KSS14, (A1)–(A5) in Appendix A). The pseudo-spectral method with the second order predictor-corrector time-integration scheme is used. Water droplets are treated as Lagrangian point particles whose position, velocity, and radius are traced inside the Eulerian grid (cf. equations (9)–(11) in KSS14, (A6)–(A8) in Appendix A). Droplet motion includes effects of gravity, inertia, and Stokes drag. Droplet growth or evaporation is calculated by applying the local value of the supersaturation (equation (12) in KSS14). Droplets smaller than 5 μm are treated as weightless tracer particles. Condensation rate within Eulerian grid cells is calculated by including contributions of all droplets within a given cell. The equations are solved in the triply periodic computational domain of $(1.024 \text{ m})^3$ with the grid length of 1 mm. The same time step is used in both Eulerian fluid-flow and Lagrangian droplet models.

The initial conditions follow the setup applied in KSS14 as well. A slab of the initially supersaturated (at 2%) cloudy volume is positioned in the center of the domain, as shown in the top left plot of Figure 1. The slab

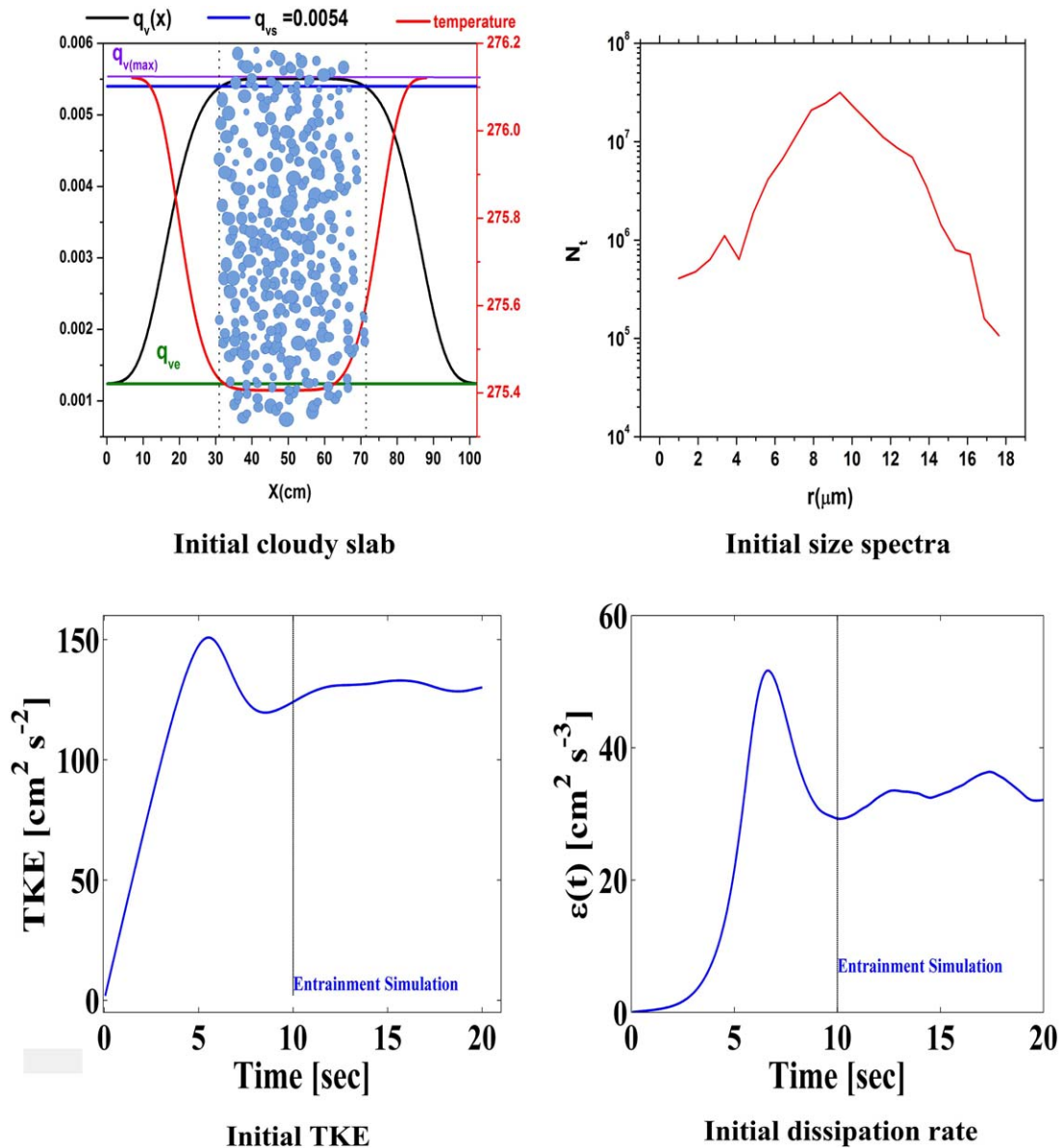


Figure 1. (top left) Initial distributions of thermodynamic variables across supersaturated cloud slab and (top right) initial DSD from aircraft observations. (bottom left) Bottom plots show evolutions of the TKE and (bottom right) volume-averaged TKE dissipation rate for a forced simulation without droplets with vertical lines showing start time of the unforced simulation with droplets discussed in this paper.

is assumed to be aligned in such a way that the gravity is along the slab and droplets initially sediment within the slab. Initial thermodynamic conditions for the model are selected from observations in cumulus clouds conducted on 3 November 2011 (during research flight RF45) at 5.0 km altitude (these will be discussed later in the paper). Droplet number concentration (N_d) in the core of the cumulus cloud was observed around 430 cm^{-3} with the mean droplet radius of $9.2 \mu\text{m}$. The initial size distribution of droplets in the cloud slab is depicted in top right plot of Figure 1. This observed undiluted DSD is used in the model to randomly distribute droplets into a cloud slab. The mean droplet concentration implies that the DNS tracks over 175 million droplets throughout the simulation. The environmental temperature and relative humidity (RH) at the observation level were 2.5°C and 22%, respectively. These are used to set the conditions away from the cloud slab (see Figure 1). These initial conditions correspond to the fluid mixing time scale of around 7 s (taking the length scale of 1 m and the initial TKE dissipation of about $33 \text{ cm}^2 \text{ s}^{-3}$) and a similar time scale of droplet evaporation.

Initially, a statistically stationary turbulent flow field as in Kumar *et al.* [2012, 2013] and in KSS14 is prescribed over the entire computational domain to let the droplets move and mix with the dry air. The initial flow field comes from a forced simulation without droplets that reach statistically stationary state as illustrated in bottom plots of Figure 1. Since no additional forcing is included in the simulations except for the one resulting from droplet evaporation and accompanying latent heating, (i.e., as in the set D in KSS14), the turbulence is expected to decay with time as the slab mixes with the subsaturated ambient air and the homogenization of the entire volume is anticipated. Note that such a decaying turbulence setup is different from the one considered in Andrejczuk *et al.* [2004, 2006, 2009]. Andrejczuk *et al.* considered initial velocity perturbations at large scales only, and the homogenization proceeded through the development of smaller scales of motion as the turbulent kinetic energy (TKE) was transferred through the inertial subrange toward molecular dissipation. Such a setup followed the dry turbulence case of Herring and Kerr [1993].

The above discussion is illustrated in Figure 2 that presents X - Y distributions of the TKE (left plots) and enstrophy (right plots) at a randomly selected horizontal plane at 1, 5, and 10 s. Note, that the TKE is associated with the largest scales of the flow, whereas enstrophy, a quantity based on velocity gradients, dominates the smallest scales. The figure shows that the small-scale turbulence initially fills the entire domain, that is, inside as well as outside of the cloudy slab. As the simulation progresses, TKE is reduced due to molecular dissipation with the local extrema reduced by a factor between 2 and 3 from 1 to 10 s. The enstrophy extrema decrease in a similar way. Evolution of TKE and enstrophy pdfs (Figure 3) shows that the initially wide pdfs become narrow. TKE recovers between 5 and 10 s, likely because of the flow structures driven by evaporative cooling as discussed later in the paper. A secondary TKE peak is evident at 10 s. The analysis discussed in the present study pertains to this TKE transitioning stage with the expectation that it reveals features similar to the turbulent entrainment and mixing in natural clouds.

The simulation output data from the Eulerian frame contain the flow velocities, temperature, water vapor mixing ratio, domain-averaged TKE, and TKE dissipation rate. Lagrangian droplet scheme provides data for all fields related to the droplet movement and growth/evaporation affected by turbulent flow fields, that is, droplet position, velocity, radius, as well as the local supersaturation and temperature.

3. Results

3.1. Evolution of Bulk Mixing

3.1.1. Model Fields During Turbulent Stirring

Figures 4–6 illustrate spatial distributions of various fields at a randomly selected X - Y plane for time 1, 5, and 10 s, respectively. The plots show the droplet concentration, mean radius, and the DSD standard deviation (referred to as the spectral width throughout the manuscript) all calculated based on the averaging over 1 cm³ volume, that is, typically using several hundreds of droplets. In addition, fields of the vertical velocity, temperature, and water vapor mixing ratio are also shown. At 1 s (Figure 4), only the very edge of the cloud slab is affected by the mixing, but the development of larger-scale structures is apparent. Droplet concentration shows significant fluctuations, “droplet clustering,” with maximum values close to twice the mean concentration in small areas inside the cloud slab, and with virtually no change of the mean radius and spectral width. This is arguably in response to the interplay between droplet inertia and droplet sedimentation (see discussions in Shaw *et al.* [1998], Grabowski and Vaillancourt [1999], and Shaw *et al.* [2003], among many others). Additional sensitivity simulation (not shown) reveals that these small-scale fluctuations become stronger when gravitational acceleration is removed and only droplet inertia and Stokes drag affect droplet motion. Cloudy volumes near the very cloud edge are strongly influenced by entrainment/mixing of the dry air. These volumes feature significant reduction of the droplet number concentration, resulting in reductions of the mean droplet radius (due to evaporation) and decreases of the DSD spectral width. Note that the latter is possible only when some of the droplets evaporate completely because a simple shift of the droplet spectrum due to evaporation leads to the increase, not decrease, of the spectral width. The mean droplet radius near slab edges approaches zero showing that many droplets evaporate completely. Development of relatively large-scale (i.e., comparable to the domain size) structures in the velocity field is also apparent. It has to be emphasized, however, that unlike updrafts and downdraft in real clouds that lead to droplet growth and evaporation and can lead to activation of new droplets [e.g., Brenguier and Grabowski, 1993], these vertical motions have no effect on droplet radius in the unstratified DNS discussed here. Such an effect can be included through the supersaturation equation (i.e., providing the vertical-velocity source for the supersaturation as in

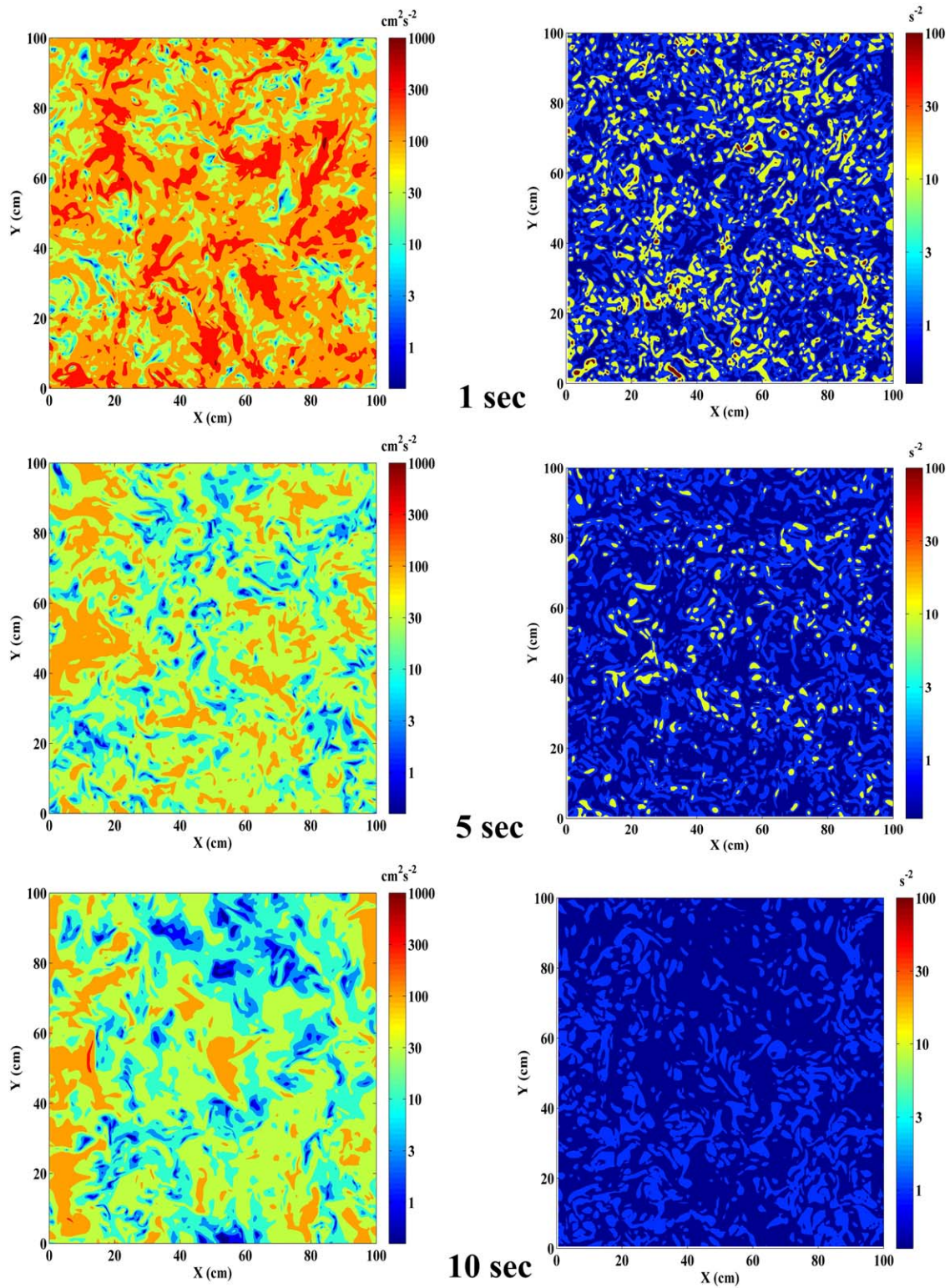


Figure 2. (left plots) Two-dimensional x-y distributions of the TKE and (right plot) the enstrophy at a randomly selected horizontal plane at 1, 5, and 10 s in top, middle, and bottom plots, respectively.

Valliancourt et al. [2001]), but it is excluded from the simulation described in the present study. Droplet vertical velocity shown in the right middle plot suggests that downdrafts are present in regions where evaporation leads to the cooling as shown in the bottom left plot of Figure 4.

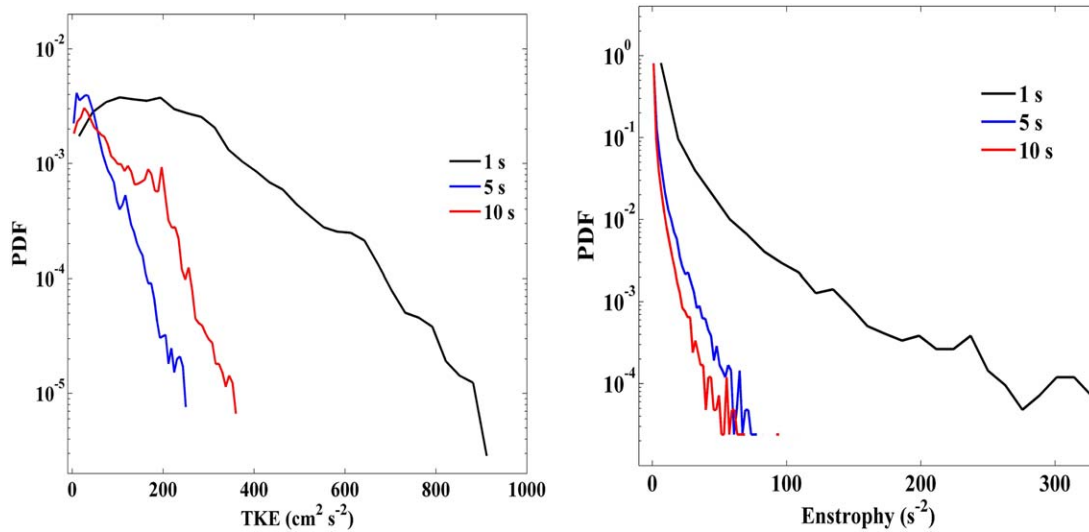


Figure 3. Probability distribution function for TKE and enstrophy for 1, 5, and 10 s.

Figure 5 shows the same fields as in Figure 4, but at 5 s of the simulation time. Formation of large-scale structures and spreading of the cloudy volume is apparent. However, the simulation is still far from the small-scale homogenization and considerable fraction of the domain remains droplet free. Concentration fluctuations similar to that at 1 s are evident (e.g., around $x = 40$ cm, $y = 60$ cm), but there are also significant volumes with partially evaporated droplets. For instance, top left corner features regions of reduced droplet concentration and mean radius. This arguably results from the partial evaporation of large droplets (i.e., reducing the size and increasing the width) combined with a complete evaporation of the smallest droplets in the distribution (hence the reduced concentration). The temperature and moisture fields show large structures characterized by significant gradients with jumps comparable to the initial difference between cloudy and cloud-free volumes, as one might expect in the turbulent stirring. Significant small-scale variability of the spectral width is seen in locations where there are accumulations of droplets through inertial clustering while large eddies with dry and warm air penetrate in the vicinity (e.g., see the area within the red square at center part of the plots). This leads to a subsequent small-scale mixing with partial droplet evaporation causing slight increase/decrease of the moisture/temperature. This effect introduces small-scale fluctuations in the temperature and moisture fields in addition to the turbulent stirring and molecular mixing processes.

The temperature and water vapor fluctuations across the entire slab are significantly larger at 5 s than at 1 s. This is a result of subsaturated air from the environment penetrating the cloudy volume and leading to the stirring of initially separated cloudy and cloud-free volumes. In some regions (see the yellow rounded squares in top left corners of all plots), there is a significant evaporation of cloud droplets as signified by the lower droplet number concentration, reduction in mean droplet radius, and fluctuating spectral width with updrafts located in close proximity of downdrafts.

At 10 s (Figure 6), there is hardly any cloud-free volume left, at least at the cross section selected. However, the small-scale fluctuations among fields shown in the figure remain significant. Droplet concentrations are lower in agreement with the bulk dilution of the cloudy volume and the spread of the cloudy slab. Droplet radii are smaller due to the mean evaporation and there seems to be more small-scale regions with increased spectral widths. There are, however, some volumes where the droplet concentration, mean radius and spectral width all remain close to the initial values, e.g., in the center of the domain. Such volumes are often in close proximity to diluted volumes (i.e., with reduced droplet concentrations and mean radii and increased spectral width). Droplet evaporation and its impact on the buoyancy field leads to the formation of large-scale velocity perturbations such as an area of an updraft in the left side of middle right plot Figure 6. We noted a secondary peak in the TKE PDF in Figure 2a, likely associated with the generation of those large-scale coherent velocity perturbations.

The temperature fluctuations at 10 s are still large, perhaps even larger than at 5 s. This is again because of the entrainment of cloud free air from outside of the slab. The entrained air seems to form a coherent

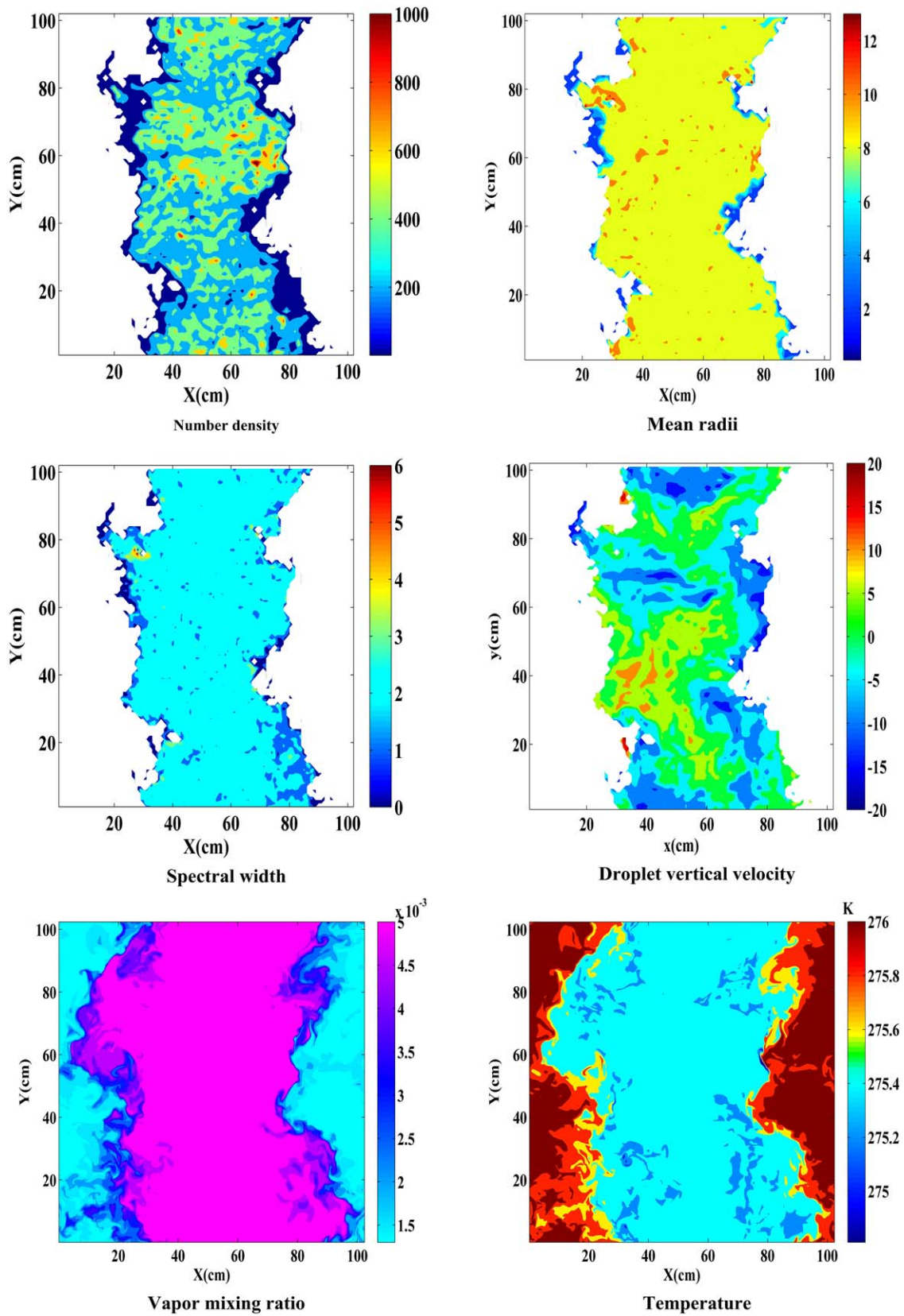


Figure 4. Two-dimensional distributions of microphysical parameters (N_d , r_m , σ , vertical velocity, q_v , and temperature) at randomly selected x - y plane from DNS data for 1 s.

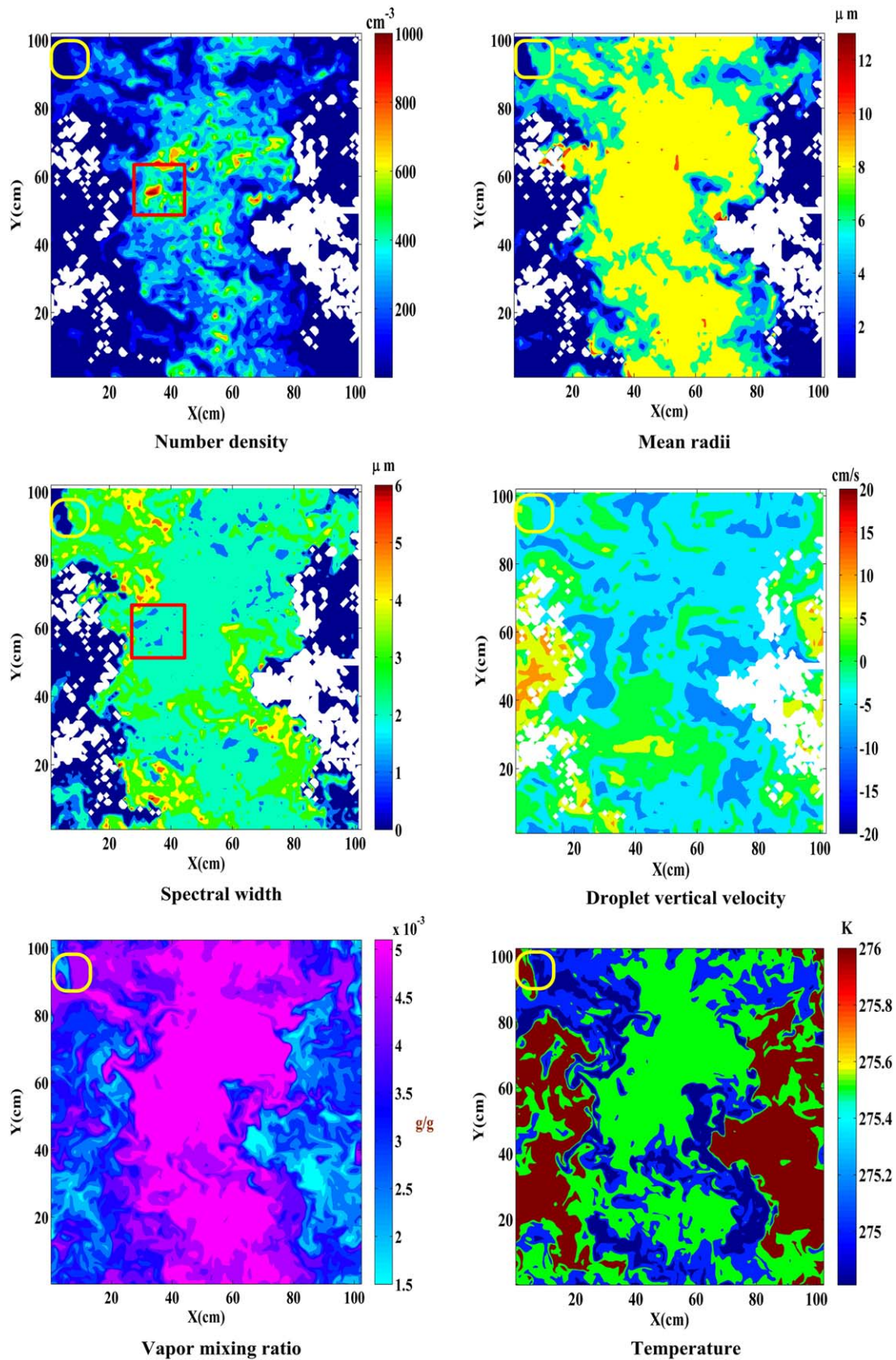


Figure 5. As in Figure 4 but at 5 s.

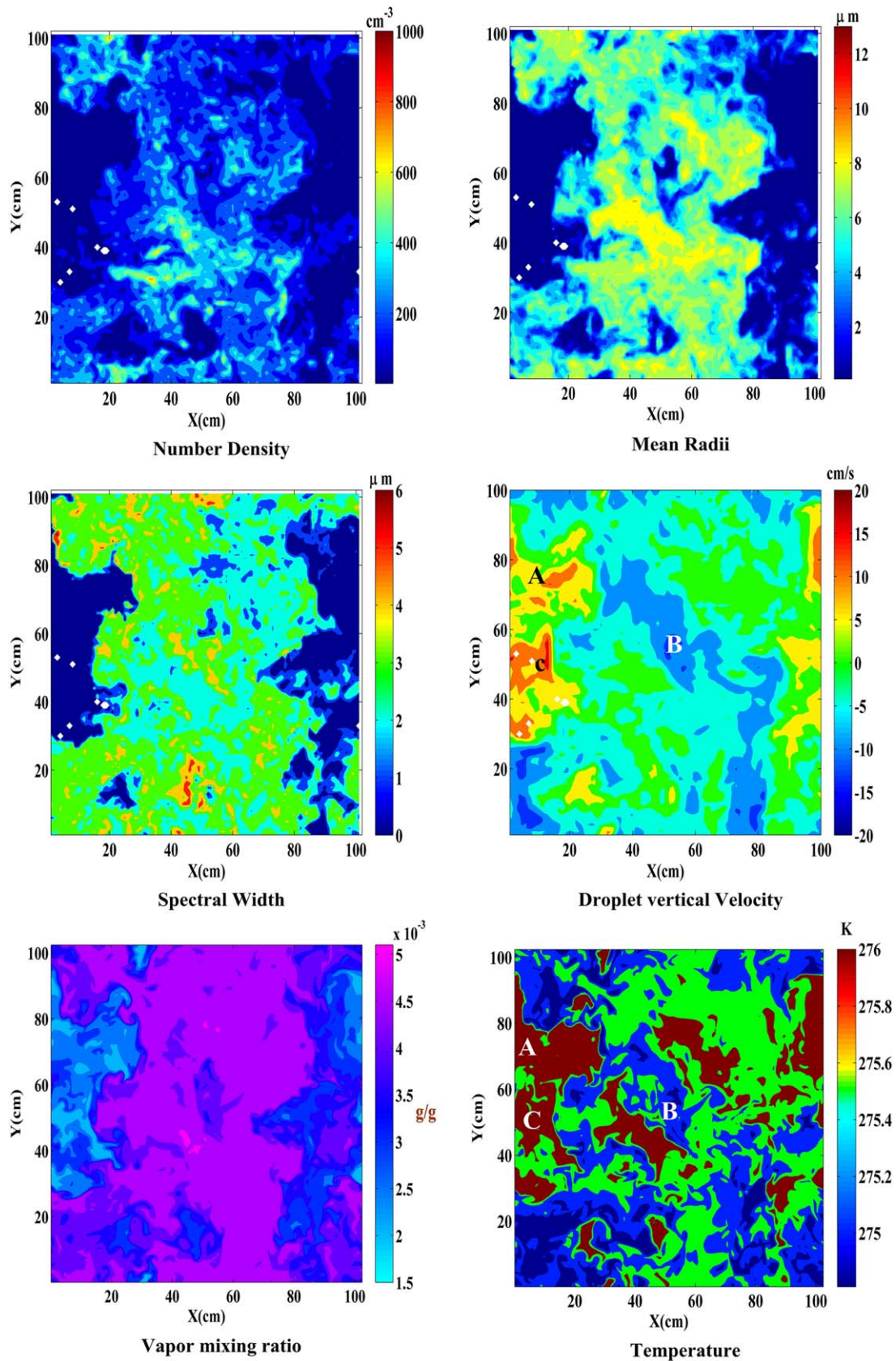


Figure 6. As in Figure 4 but at 10 s.

pattern in the temperature and vertical velocities fluctuations, with cool downdrafts (B) and warmer updrafts (A and C). The warm regions have higher droplet mean radius and relatively higher droplet number concentration. The maximum spectral width occurs in regions with large spatial gradients in the number concentration and temperature (e.g., in small areas A and B). There are relatively small spatial fluctuations of the moisture fields, likely due to the homogenizing effect of droplet evaporation.

Figure 7 shows the same fields as Figure 5 (i.e., at 5 s) but with the data averaged over 8 cm^3 volume. As one might expect, averaging droplet data over about an order of magnitude larger volume leads to a significant reduction of small-scale fluctuations. This effect is most dramatic in the droplet concentration where the maxima evident when averaged over 1 cm^3 are reduced by half or more in the 8 cm^3 averaging. This is arguably because of the gradual reduction of the droplet clustering with the increase of the spatial scale. Differences in other microphysical fields (e.g., the mean radius, spectral width) are less dramatic. Differences for the temperature and water vapor mixing ratio are surprisingly small.

3.1.2. Evolution of the Whole-Domain Statistics

Evolution of parameters describing global mixing characteristics is shown in Figure 8. The figure shows the domain-averaged TKE and TKE dissipation rate together with the total number of droplets, droplet mean radius, moist static energy (MSE) variance, spectral width as well as the mean temperature during the initial 12 s of the simulation. Because of a complete evaporation of some droplets, the total number of droplets decreases by about 34%.

The mean radius increases slightly initially due to the growth of the droplets owing to the prescribed initial supersaturation inside the cloud slab (so does the mean temperature), but subsequently the mean temperature, the mean radius, and the total number of droplets all decrease. The mean TKE and TKE dissipation rate decrease sharply in the initial few seconds and then level off. There is a notable increase in TKE from 8 to 12 s, arguably associated with the formation of coherent flow structures apparent in Figure 6. The MSE variance continuously decreases with time. During the first 12 s, the mean radius is reduced from about 9.4 to about $4.3 \mu\text{m}$. The mean spectral width increases from about 2.2 to about $4.0 \mu\text{m}$ during the initial 10 s and then decreases slightly. Since the change of the relative dispersion (i.e., the ratio of the spectral width to the mean radius) is inversely proportional to the change of the radius squared [Liu et al., 2006], the approximate doubling of the spectral width is consistent with approximate halving of the mean radius.

It should be stressed that the mean conditions at the time of 12 s shown in Figure 8 are not the final homogenized state of the system. The initial thermodynamic conditions of cloudy and cloud-free air together with the 1/3 fraction of the domain covered initially by the cloudy slab dictate that all droplets eventually evaporate. Owing to the weak turbulence after a few initial seconds, it takes another several tens of seconds to evaporate all droplets (not shown). However, our focus is on the active mixing during the first dozen of seconds of the simulation, after the entrainment of subsaturated droplet-free air into the cloud.

Figure 9 shows evolution of the total number of droplets plotted as a function of the mean (i.e., domain-averaged) droplet radius, both normalized by the initial values. Such a diagram was introduced by [Burnet and Brenguier, 2007] and subsequently used in analyses of DNS simulations carried out in [Andrejczuk et al., 2004, 2006, 2009]. On this diagram, the isolines of the constant cloud water content are hyperbolas (shown as thin solid lines in Figure 9), the horizontal line represents extremely inhomogeneous mixing (reduction of the number of droplets without change of the mean radius), and the vertical line corresponds to the homogeneous mixing (reduction of the mean radius with no change of the number of droplets). Symbols mark different times as the mixing progresses with the corresponding Damkohler numbers D_a shown by colors and shapes of the symbols. Theoretically, homogeneous (extremely inhomogeneous) mixing corresponds to the limit of $D_a \ll 1$ ($D_a \gg 1$). The figure shows that mixing seems to follow the homogeneous mixing line within a few first seconds. The initially homogeneous mixing does not seem to be consistent with the estimated D_a as $D_a \sim 1$. This is perhaps because of the initial supersaturation within the slab that leads to growth of some droplets compensating evaporation of others due to mixing. Another possibility is that the Damkohler number considerations apply to situations when the volume under consideration becomes homogenized and the thermodynamic equilibrium is approached. This is clearly not the case very early in the simulation when droplets have just started to adjust to local conditions.

At later times, mixing transitions toward the intermediate mixing along the diagonal of the diagram.

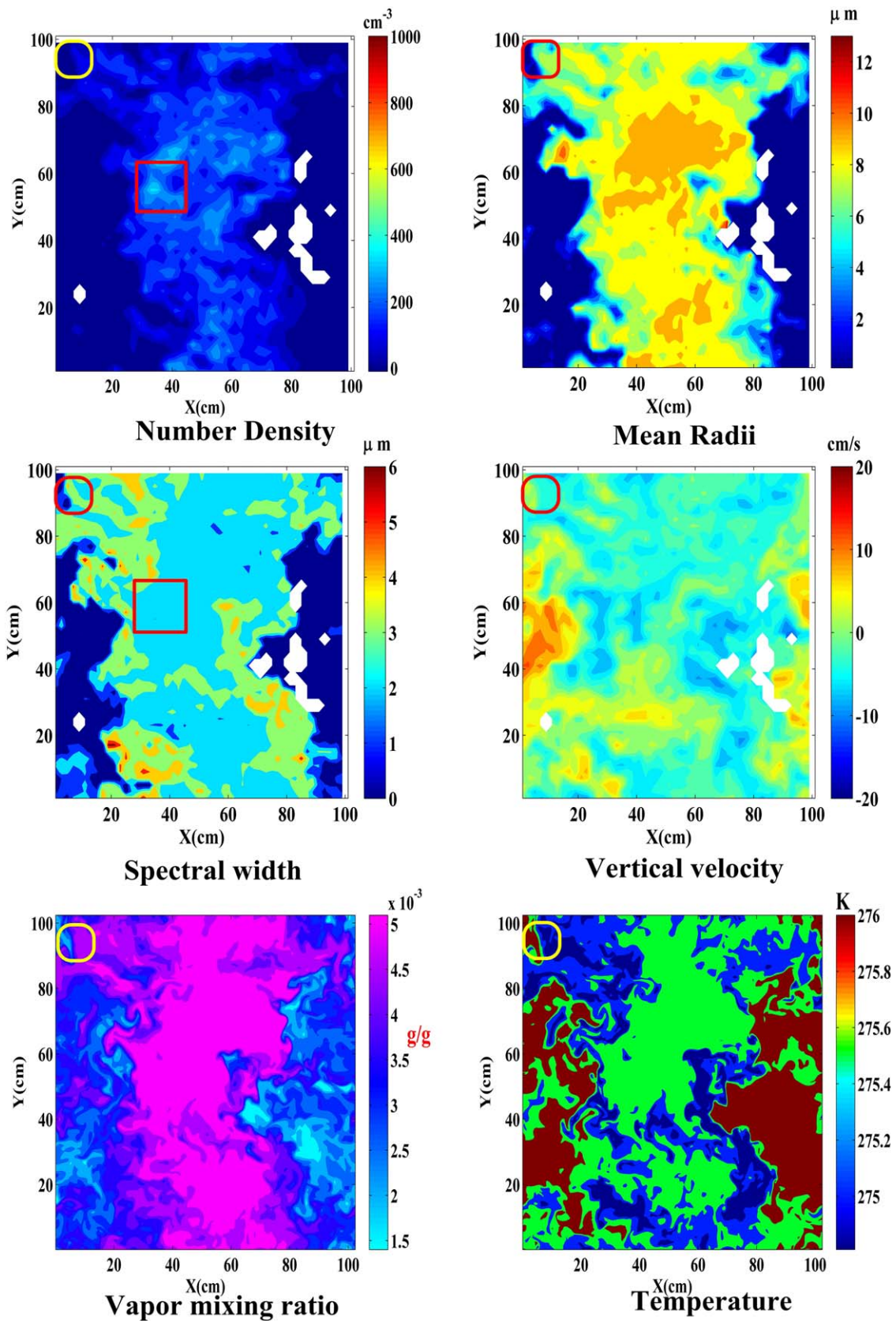


Figure 7. As in Figure 5 but with data averaged over volume of 8 cm^3 .

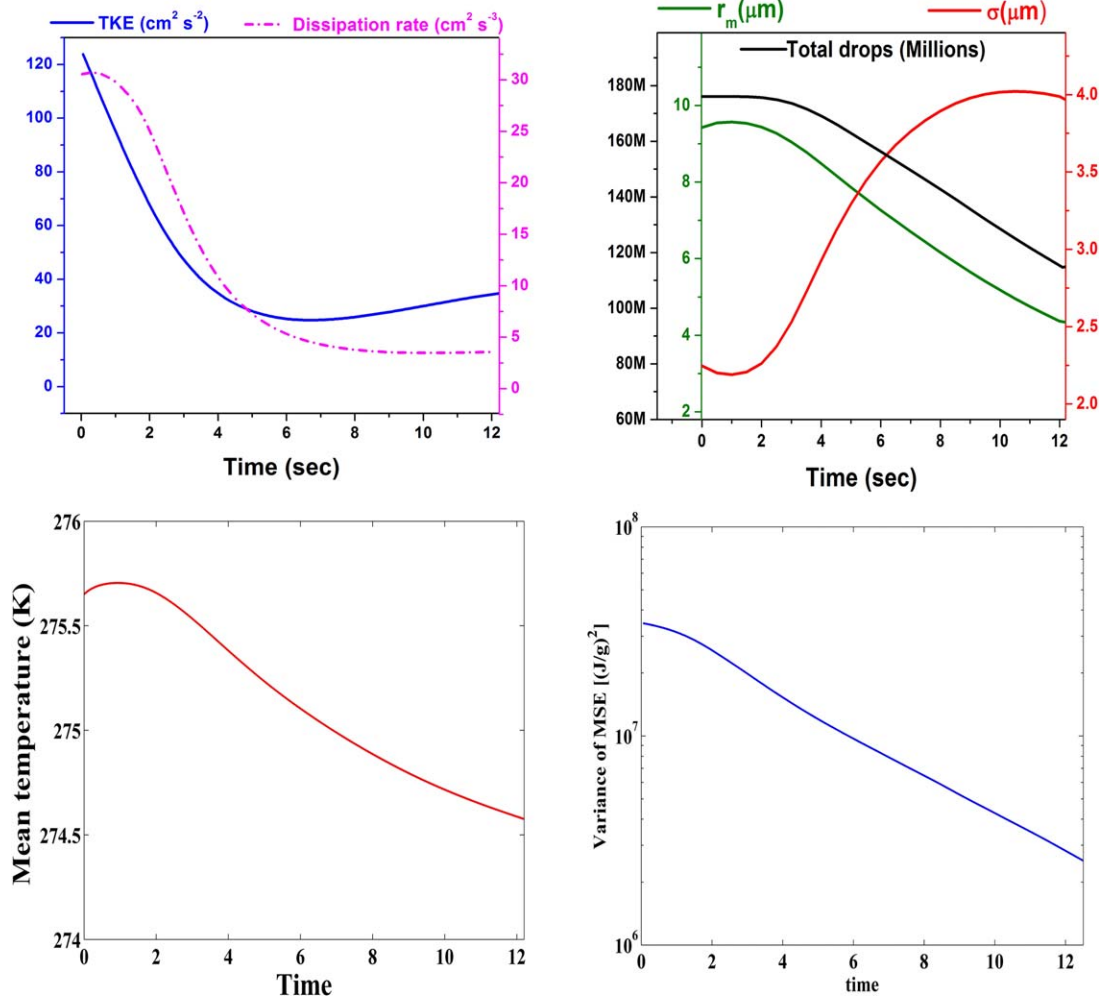


Figure 8. Evolution of parameters describing domain-averaged characteristics for the first 12 s of the simulation. (top left) TKE and dissipation rate; (top right) the mean radius, spectral width and total number of droplets with nonzero radius; (bottom left) the mean temperature; (bottom right) variance of the moist static energy (MSE).

3.1.3. Covariability of Microphysical Parameters

Figure 10 shows contour-plots documenting the covariability between the local (i.e., averaged over 1 cm³ volume) droplet concentration, mean radius, and spectral width at 1, 5, and 10 s of the simulation and at a randomly selected X-Y plane (results from other planes are similar; averaging over the entire computational domain volume is cumbersome due to the amount of data). In addition, several datapoints along a pencil-like cut across the observed cloud (to be discussed later) is also shown as magenta dots in plots corresponding to DNS simulation at 1 s.

At 1 s, the plots are dominated by the initial conditions, that is, the droplet concentration shows a large spread (due to the effect of inertia as already noted in Figure 4) with the mean radius and spectral width mostly close to the initial conditions (around 9 and 2 μm, respectively). Significant evaporation of some droplets is also apparent (e.g., the mean radius below 5 μm in the bottom left plot).

The reduction of the mean droplet concentration is possible either through a simple dilution (i.e., increasing the cloudy volume as evident in Figures 4–6 and in the maximum concentrations in the top and bottom rows in Figure 8) or by evaporation of the smallest droplets in the DSD (i.e., partial evaporation). Both can lead to the spread of the mean radius and spectral width at low droplet concentrations. The partial evaporation leads to a complete removal of small droplets, with the remainder showing low spectral width. On average, spectral width seems to increase and the mean radius to decrease with reduction of the droplet concentration. For the spectral width, the trend seems to reverse at low droplet concentrations, best

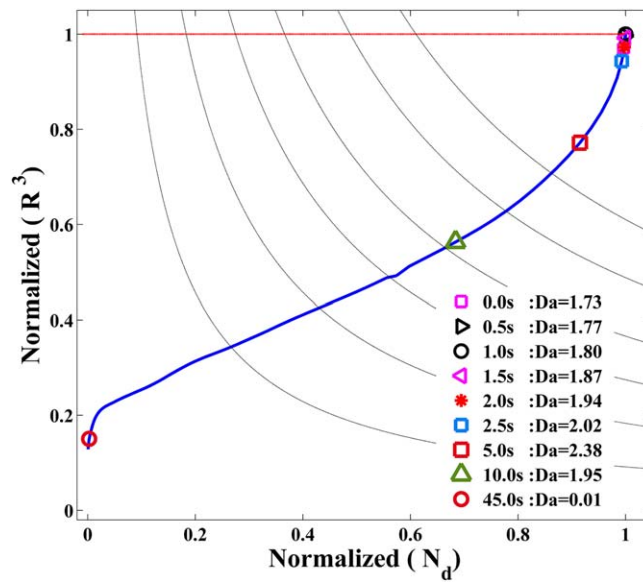


Figure 9. Mixing diagram applying droplet properties averaged over the entire domain. The Damköhler numbers ($Da = \tau_{mix} / \tau_{phase}$) at various times are shown by corresponding symbols. The τ_{mix} is fluid time scale and the $\tau_{phase} = (1/4\pi DN_d t)$ is the phase relaxation time [Kumar et al., 2012].

1 s, perhaps because the still undiluted core and cloud-edge flow structures (cf. Figures 4–6) bear the best similarity to the structure of a cumulus cloud at the developing (growing) stage.

3.2. Flying Imaginary Aircraft Trough DNS Domain

Figure 11 shows data from a transect of the computational domain perpendicular to the initial slab for $z = 50$ cm and $y = 57$ cm for $t = 1, 5,$ and 10 s. One can consider these data as obtained by an imaginary aircraft flying through the computational domain. The sample volume has linear dimensions of 1, 3, and 1 cm in $x, y,$ and z directions, respectively, that is, averaging over 3 cm^3 volume. This is closer to the sample volume of aircraft observation at 10 Hz (around 4.4 cm^3) than the 1 cm^3 used in Figures 4–6 and 10. The aircraft sample volume V of the FSSP is calculated as: $V = DOF * BD * TAS / R$, where DOF is the depth of field equal to 2.2 mm, BD is the beam diameter equal to 0.2 mm, TAS is the true air speed (around 100 m s^{-1}), and R is the sampling rate (10 s^{-1} for 10 Hz observations). This gives $V = 4.4 \text{ cm}^3$. Since aircraft observations involved 1-D transect of a cloud, we compare data from a cloud transect with similar data from a DNS domain transect.

The left plots in Figure 11 show variations of microphysical parameters, namely, the droplet number concentration, spectral width of DSD, and mean droplet radius along the x axis (i.e., in the direction perpendicular to the initial slab) resulting from averaging DNS data over 3 cm^3 sample volume. Selected DSDs for different X -positions are shown in the middle plots. The right plots show data points from the transect applying the mixing diagram that displays the mean radius cubed (r_m^3) versus the number density (N_d); [Burnet and Brenguier, 2007]. Similar diagram was used in analyses of DNS simulations in [Andrejczuk et al., 2004, 2006, 2009] and earlier in this paper applying total number of droplets rather than the droplet concentration. Applying concentration rather than the number of droplets changes the homogeneous mixing line because the total volume combines volumes of cloudy and cloud-free air, and the concentration does change even if the number of droplets does not. The diagram was proposed by Burnet and Brenguier [2007] and it was also used in the analysis of the large eddy simulations discussed in Jarecka et al. [2013a, 2013b]. The starting point of the mixing diagram in the top right corner corresponds to the highest LWC along the pass through the cloudy slab, with the corresponding droplet concentration and radius applied to normalize values derived in other locations along the transect. We decided to apply such a normalization to remove the impact of reduced droplet concentrations and radii at 5 and 10 s as evident in the left plots of Figure 11. The horizontal line on the mixing diagram represents reduction of the droplet concentration without any change of the droplet radius and thus it marks the extremely inhomogeneous mixing. The blue

evident at the time of 10 s (Figure 10c). This seems to agree with the homogeneous evaporation of a droplet population that first leads to the increase of the spectral width as spectrum shifts toward smaller sizes, but then the smallest droplets from the spectrum evaporate completely as the evaporation continues. It follows that the spectral width and mean radius are nonlinearly related when the initial DSD has large width.

The magenta dots in left plots (i.e., for DNS results at 1 s) represent in-cloud observations at 10 m resolved scale (10 Hz) from the research flight RF45 during CAIPEEX. Amazingly, the observation points seem to follow similar scatter pattern as in DNS despite the dramatic difference in the resolved scales (tens of meters in observations and centimeters in DNS). The agreement seems to be the best for DNS at

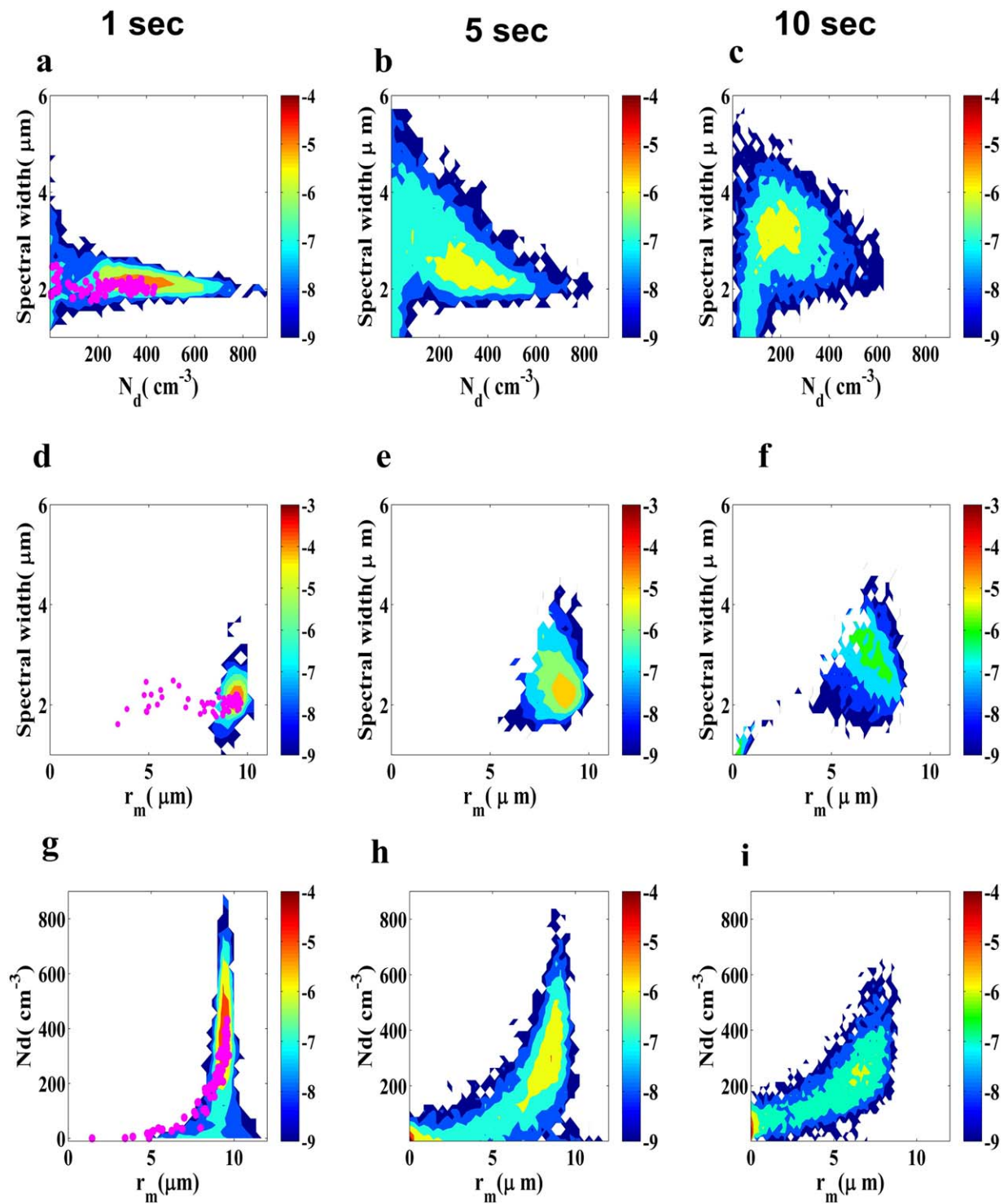


Figure 10. Contours of the probability density function illustrating relationships among the droplet concentration, mean radius, and spectral width for times 1, 5, and 10 s. in left, middle, and right plots, respectively. The magenta dots in left plots represent in-cloud observations from CAIPEEX.

line represents homogeneous mixing with the relative humidity of the initial cloud-free air outside of the cloudy slab. Homogeneous mixing lines for other humidities (85% and 98%) are also shown.

At 1 s (top row in Figure 11), the mixing between cloudy air from the slab and its unsaturated environment is limited to the slab edges. Inside the slab, mean droplet radius and spectral width are close to the initial

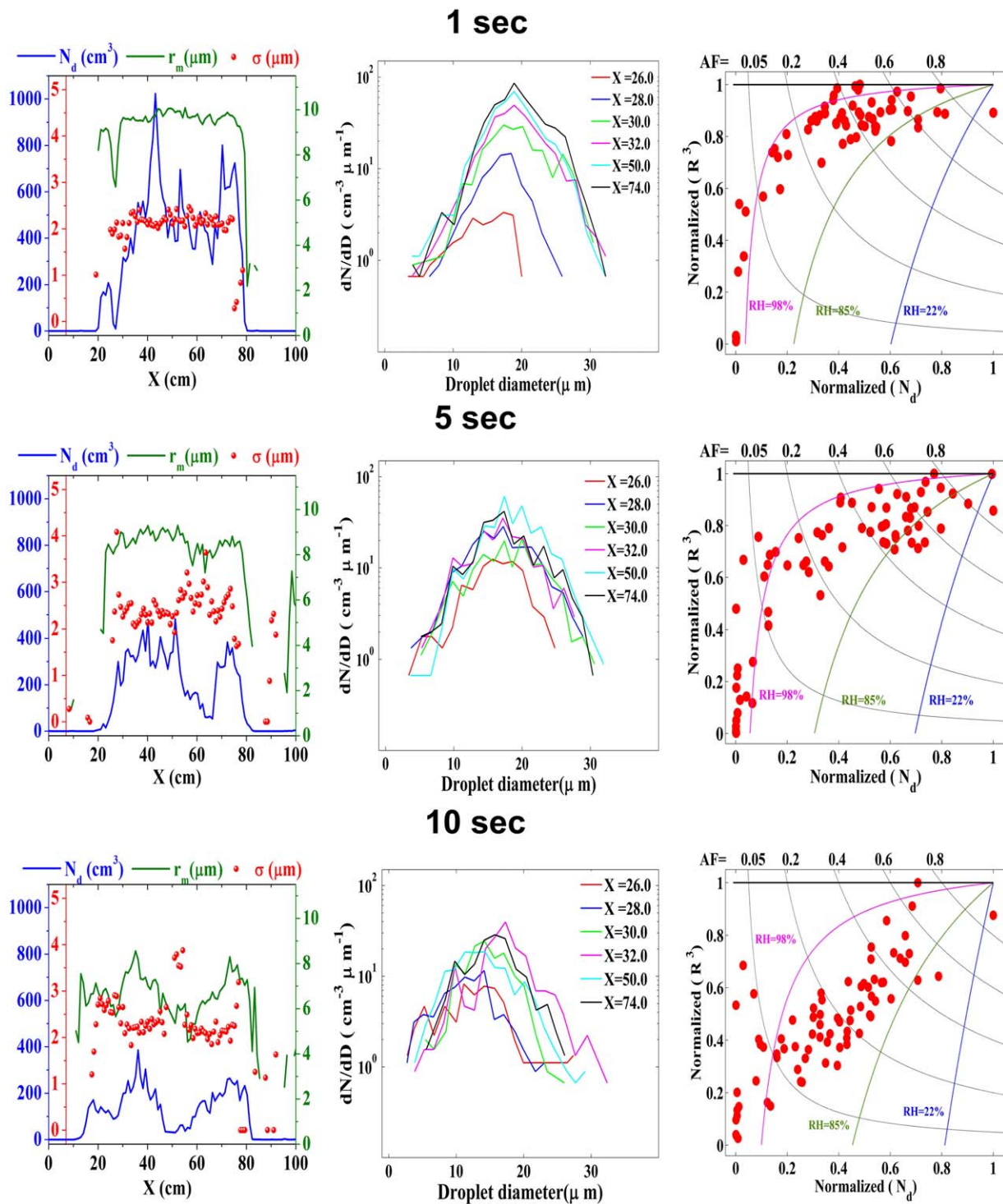


Figure 11. Microphysical parameters along a track of imaginary aircraft flying through the DNS domain. Top, middle, and bottom rows of plots show data for 1, 5, and 10 s, respectively. Plots in the left column show droplet number density, mean radius, and spectral width along the track. Selected DSDs at different locations along the track are shown in the middle plots. The right plots show mixing diagrams at times 1, 5, and 10 s. Data averaged over 3 cm^3 .

values (see Figure 8), and fluctuations of the droplet concentration are arguably due to inertial effects leading to the droplet clustering. Mixing around $x = 26 \text{ cm}$ strongly reduces droplet concentration with some reduction of the mean radius and some fluctuations of the spectral width. Examples of DSDs (top middle plot) show reduction of the droplet concentration with rather small changes of the mean radius.

The mixing diagram (top right plot) shows points clustered along the extremely inhomogeneous mixing line for the normalized droplet concentrations larger than 0.4 and with significant fluctuations. These fluctuations are likely the result of droplet clustering, not entrainment and mixing. Only for the normalized droplet concentrations smaller than about 0.4, the normalized droplet radius rapidly decreases with data points aligned along what might be argued as the homogeneous mixing line. This is consistent with the very small spatial scales in the DNS simulation leading to the short turbulent mixing time scale $L^2/\epsilon^{\frac{1}{3}}$, where L and ϵ are the relevant length scale and the eddy dissipation rate (e.g., around 0.5 s taking $L = 1$ cm and the $\epsilon = 10 \text{ cm}^2 \text{ s}^{-3}$). However, the homogeneous mixing line along which the DNS points seems to be aligned corresponds to a significantly higher RH than the initial RH of the cloud-free air of 22%.

At 5 s (middle row in Figure 11), the entire cloudy slab shows mean dilution, consistent with Figure 5. The mean number concentration and droplet radius within the slab are reduced, and there are significant fluctuations, similar to those at 1 s. Evaporation of cloud droplets leads to the reduction of the radius and number concentration, and a noticeable increase of the spectral width. One can distinguish several zones where the properties are rapidly changing. In some places, there are no droplets and thus the green mean radius line is not continuous. DSDs do not seem to differ strongly when plotted at randomly selected points and applying logarithmic scale on the vertical axis. The mixing diagram (the right plot) shows points creating a pattern similar to that 1 s, but with large reductions of the normalized radius starting from the normalized concentration of 0.6.

Plots at 10 s (bottom row in Figure 11) show progress of the cloudy slab mean dilution. The mean radius fluctuates along the pass from around 4 to around 8 μm , so does the spectral width. DSDs vary significantly along the pass, but in a way that does not allow a clear interpretation. Some spectra show the shift toward smaller sizes, and some are similar to the initial spectrum but with reduced concentration. The alignment of points on the mixing diagram is more ambiguous because of the significant scatter.

Figure 12 shows similar data to Figure 11, but using DNS data averaged over 8 cm^3 . The motivation comes from significant differences evident in two-dimensional plots of fields averaged over 1 and 8 cm^3 discussed previously (cf. Figures 5 and 7). As the Figure 12 shows, however, the averaging has relatively small impact on the overall conclusions that one may draw using mixing diagrams. The number of datapoints is obviously reduced with 8 cm^3 , but the key features highlighted in the discussion above remain unchanged, especially for the mixing diagram.

In summary, DNS show a gradual dilution of the cloudy slab as the simulation progresses accompanied by significant fluctuations of microphysical parameters. Initially, the concentration fluctuations are arguably due to inertial effects, later aided by larger-scale entraining eddies whose impact on the slab structure is evident in Figures 4–6. Mixing diagrams can be argued to show mixing not far from the homogeneous one, but with the relative humidity significantly larger than the humidity of the cloud-free air outside of the cloudy slab at the onset of the simulation as previously reported from CAIPEEX observation in Bera *et al.* [2016b].

4. Analogy Between DNS and In Situ Aircraft Observations of Natural Clouds

We use in situ aircraft observations of cumulus clouds taken during the Cloud Aerosol Interaction and Precipitation Enhancement Experiment (CAIPEEX) Phase-II on 3 November, 2011. The cloud observations were performed at 5.0 km altitude with in-cloud temperature close to 2.0°C. There was no ice particle formation at that level.

Forward Scattering Spectrometer Probe (FSSP) is used on the Aerocommander aircraft to obtain DSDs with diameter between 2 and 50 μm from which the total droplet concentration, mean radius, and spectral width are derived. Relative humidity (RH) and temperature are measured from Aircraft Integrated Meteorological Measurement System (AIMMS-20) probe. The measurements applied in this study were collected at 10 Hz, that is, over a distance of about 10 m given the aircraft speed approximately 100 m s^{-1} . The cloud profiling was done with aircraft on constant altitudes at nearly 1000 ft intervals. The main emphasis in the experiment was to register the cloud drop size distributions and associated vertical velocity, temperature, and humidity along each horizontal transect across the developing cloud [Prabha *et al.*, 2011].

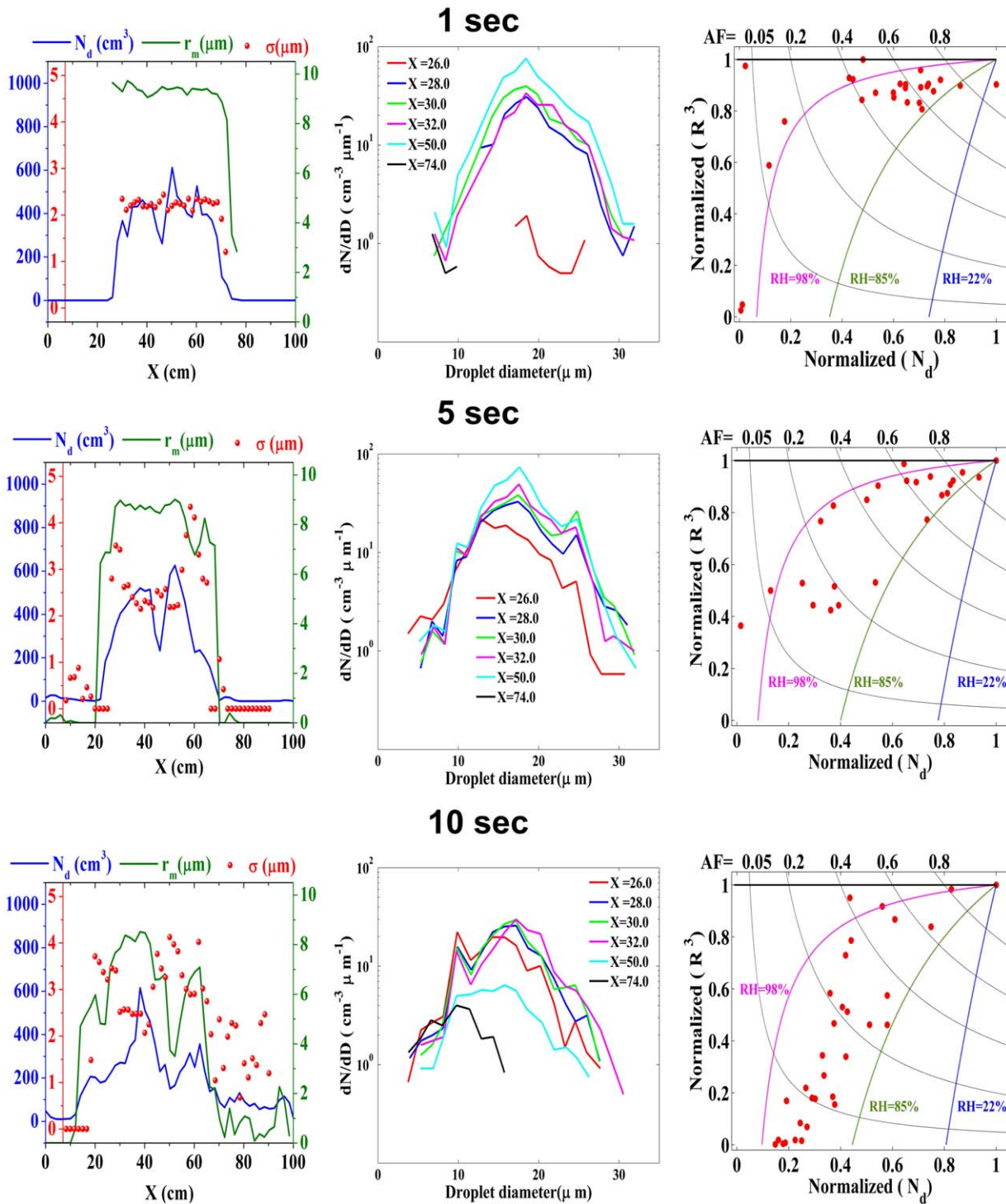
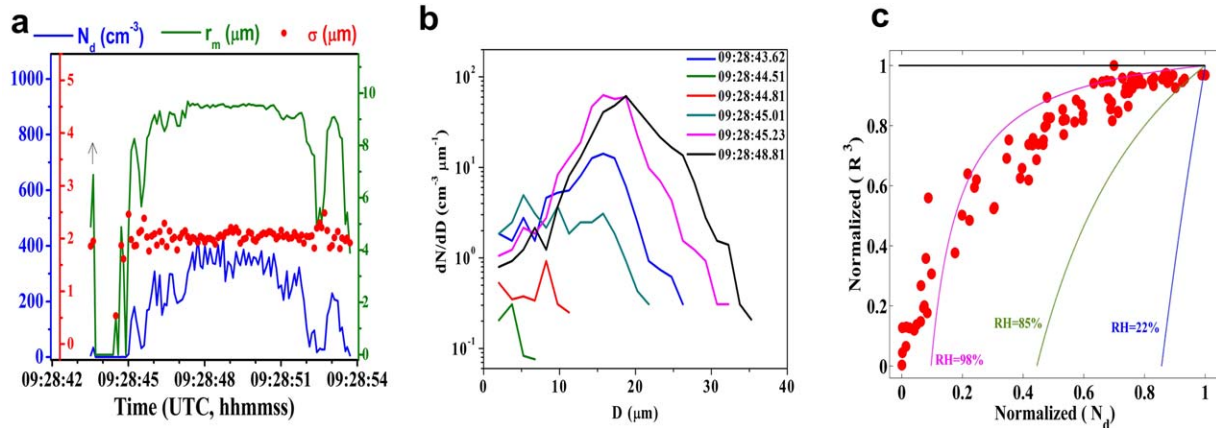
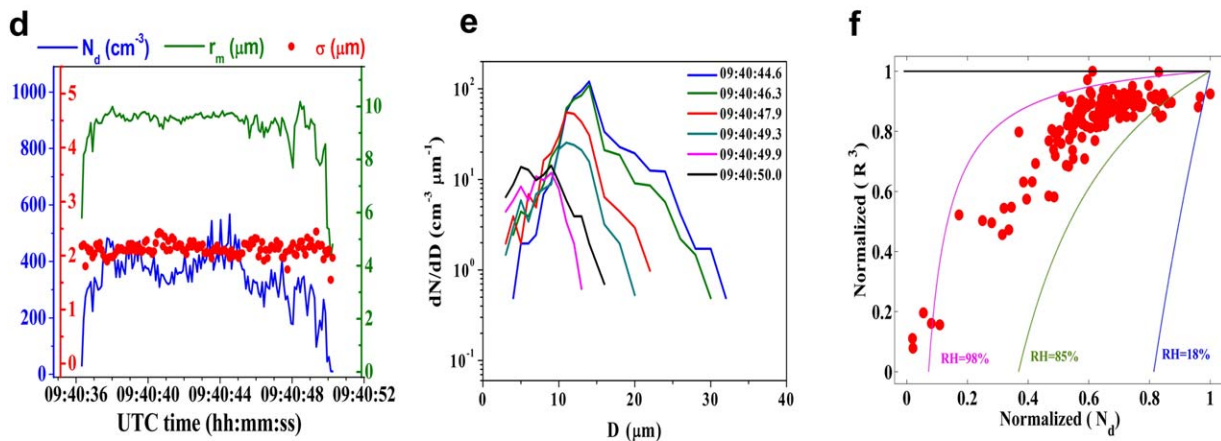


Figure 12. As in Figure 11 but using DNS data averaged over the 8 cm^3 .

Figure 13, in the same format as Figure 11, shows examples of the data obtained during two transects through a cumulus cloud at an altitude of 5.0 km and 4.8 km, respectively, for top (a-c) and bottom (d-f) plots. Left plots show the observed droplet concentration, mean radius, and the spectral width along the flight path. Droplet concentrations and radii are the highest near the center of the cloud (i.e., at 09:28:48 UTC for pass 1 and 09:40:44 UTC for pass 2) compared to the cloud edges. Droplet concentration shows significant fluctuations. However, these fluctuations cannot come from inertial effects seen in the DNS



Microphysical parameters from observation: pass 1



Microphysical parameters from observation: pass 2

Figure 13. Aircraft data from two passes through a growing cumulus cloud from CAIPEEX field program displayed in the same format as in Figures 11 and 12. The values along the flight track, DSDs, and mixing diagrams are to be compared to similar plots for the DNS data.

simulation because of around 10 m horizontal length over which the local droplet concentrations are derived. More likely these fluctuations come from the impact of horizontal variability of the vertical velocity near the cloud base (that affect concentration of activated CCN) or entrainment/mixing and activation above the cloud base. The spectral width fluctuates around $2 \mu\text{m}$ with larger fluctuations near cloud edges. These DSD parameters change significantly when one moves away from the center of the cloud. Droplet concentration and the mean radius show gradual reduction albeit with significant fluctuations. The spectral width also fluctuates significantly toward cloud edges showing values both smaller and larger than the $2 \mu\text{m}$ observed at the cloud center [Bera et al., 2016b].

The middle plots in Figure 13 show examples of DSDs along the flight track at different locations identified by the time of observation. The DSDs in the middle of the cloud show the largest droplets. The DSDs are fairly wide, with a secondary peak at small sizes suggesting recent secondary activation or mixing with highly diluted cloudy volume and thus small cloud droplets due to partial evaporation. The possibilities of secondary activation have been reported in monsoon clouds [e.g., Prabha et al., 2011]. They have also been simulated in a shallow cumulus [e.g., Slawinska et al., 2012]. Diluted DSDs are observed away from the cloud core with nearly invariant DSD [Khain et al., 2013], with smaller mean diameter and even more pronounced peak at small sizes. The DSDs suggest a complete evaporation of small droplets and partial evaporation of large drops. At cloud edges, the spectra are only at the smallest sizes suggesting close to complete evaporation of the cloud water.

Mixing diagrams corresponding to the data along the two passes are shown in the right plots (c and f). As for the DNS data, we normalize the concentration and the radius cubed by the values corresponding to the maximum LWC along the pass. Note that this is similar to the normalization by the adiabatic values in *Burnet and Brenguier* [2007] and to the normalized mixing diagrams for the DNS data with the normalization not affecting the pattern formed by data points along the flight track. The key point is that the pattern is surprisingly similar to the DNS data shown in Figure 11 at 1 or 5 s.

In summary, there are intriguing similarities between the DNS results and results of in-cloud observations from CAIPEEX, especially from the point of view of the DSDs and mixing diagrams. The next section provides a discussion of basic mechanisms that may explain these similarities.

5. Discussion and Conclusions

This paper presents results from idealized DNS simulations of cloud-edge mixing and compares key simulated features to aircraft observations of natural convective clouds. The DNS applies a fairly standard Eulerian incompressible fluid-flow model coupled to large set of Lagrangian cloud droplets. The initial conditions for the DNS follow *Kumar et al.* [2014] and they feature a cloudy slab covering approximately a third of the triply periodic computational domain of approximately 1 m^3 volume. Thermodynamic conditions within the slab and of the subsaturated air outside the slab are taken from the aircraft observations of the CAIPEEX field project and the cloud environment, respectively. The observed droplet size distribution is used to prescribe initial droplet sizes and droplets are randomly positioned within the cloudy slab. The initial flow features the stationary turbulence over the entire computational domain. The Lagrangian droplet dynamics in the decaying turbulent flow is simulated and the evolution of thermodynamic properties and droplet spectral characteristics are analyzed.

Evaporation of droplets in the unstratified DNS happens because of the resolved turbulent transport and molecular diffusion of the temperature and water vapor into the cloudy slab from the subsaturated environment. Droplet sedimentation at later stages plays some role as well (initially droplets sediment along the slab). It follows that larger-scale downdrafts in DNS develop solely because of the droplet evaporation, and updrafts form through the action of the pressure perturbations that ensure vanishing mean flow at any level due to the flow incompressibility. However, in natural clouds developing in stratified environments, vertical motions drive droplet diffusional growth or evaporation in addition to the evaporation resulting from entrainment and mixing. This effect is excluded from the DNS simulation.

The cloud-edge entrainment and mixing starts at small scales and gradually introduces larger scales of the temperature, moisture, and vertical velocity variations due to droplet evaporation and latent heating. The cloud-clear air mixing is initiated at cloud edges and subsequently expands into the slab. Large coherent structures are created that contribute to the development of preferential updraft and downdraft zones with distinct evaporation of cloud droplets (cf. Figures 4–6). The major impact is on the temperature and vertical velocity indicating that mixing is buoyancy driven due to evaporative cooling. This leads to some enhancement of the domain-averaged TKE (cf. Figure 8). We focus on early (up to about a dozen seconds) evolution of the simulated fields. Advection and molecular diffusion of the temperature and moisture from the outside of the cloudy slab leads to mean slab dilution and evaporation of cloud droplets, evident in model results at 5 and 10 s. All droplets have to eventually evaporate and the final homogenized volume is cloud-free. This is arguably similar to natural shallow cumulus clouds that evaporate at the end of their life-cycle.

In contrast, entrainment in natural convective clouds occurs due to the action of large-scale (i.e., comparable to the size of the cloud) circulations and/or eddies that result in the cauliflower shape of the cumulus cloud [e.g., *Grabowski and Clark*, 1991, 1993a, 1993b; *Grabowski*, 1993; *Brenguier and Grabowski*, 1993; *Carpenter et al.*, 1998a, 1998b, 1998c; *Zhao and Austin*, 2005a, 2005b]. These structures are driven by the vorticity dynamics at the cloud-environment interface and provide the source of the TKE that cascades across the inertial range down to the molecular dissipation at the Kolmogorov microscale [*Grabowski and Clark*, 1993a]. Aircraft observations are seldom capable in resolving the entire range of scales, from tens or hundreds of meters down to the subcentimeter scale. Although DSDs are typically derived from recordings of individual droplets (e.g., using a FSSP probe), the requirement of having a sufficient number of droplets dictates that DSD can only be estimated with confidence at spatial scales larger than a few meters. At 10 Hz (i.e., around 10 m spatial scale) as used here, the impact of entraining eddies on DSDs should be relatively well resolved.

We apply methodologies used previously in displaying aircraft observations showing variations of DSDs and DSD parameters along the flight path and applying the mixing diagram of *Burnet and Brenguier* [2007] to the DNS simulations. Overall, the DNS results show intriguing similarities to the aircraft observations in natural clouds despite dramatically different spatial scales involved: scales close to the dissipation range in DNS (up to tens of centimeters) and scales not far from the energy-containing scales in aircraft observations (tens and hundreds of meters). Perhaps a heuristic argument can be made that the two involve just different ranges in the same inertial subrange, and thus some similarities are to be expected. However, the mixing diagram as used here is often used to interpret DSD observations in natural clouds in the context of homogeneous versus inhomogeneous mixing. The distinction between various mixing types is made in such studies applying the turbulent homogenization (or mixing) time scale that considers the spatial extent of the volume under consideration [e.g., *Burnet and Brenguier*, 2007]. The time scale is dramatically different between DNS and aircraft observations, fraction of a second versus a few tens of seconds, respectively. Assuming that the droplet evaporation time scale is similar in DNS and in aircraft observations (which should be the case as DNS applies conditions taken from observations), then there should be significant differences between mixing diagrams in both cases. However, this is not the case as Figures 11–13 clearly show.

The inconsistency between estimates of the relevant time scales and the observed characteristics of mixing was recently noticed in [*Yum et al.*, 2015]. Their study presents analysis of the aircraft measurements of marine boundary layer stratocumulus clouds over the southeastern Pacific off the coast of Chile during the Variability of the American Monsoon Systems Ocean-Cloud-Atmosphere-Land Study Regional Experiment (VOCALS-REx) field campaign. Yum et al. show that the time scales of mixing and of droplet evaporation imply the inhomogeneous mixing (arguably consistent with stratocumulus low turbulence intensity), yet the observations typically imply homogeneous mixing. Yum et al. suggest a possible physical mechanism leading to such a discrepancy.

We do not have any explanation for the similarities between mixing diagrams in DNS and in cloud observations. As far as we can tell, this is the first application of the mixing diagram to the DNS-generated cloud droplet data in the same way as applied in aircraft measurements. [*Andrejczuk et al.*, 2004, 2006, 2009] apply the mixing diagram to trace evolution of the domain-averaged properties of the DSD and not the local characteristics as it is done here. Arguably, local properties of the DSD at small scales (i.e., close to the Kolmogorov scale), where individual droplets respond to their local thermodynamic environment, can evolve differently from a simple conceptual model involving mixing of two air parcels. *Grabowski* [1993] discussed idealized microscale simulations of buoyancy reversal resulting from molecular diffusion and droplet sedimentation across the cloud-clear air interface. Similarly to the mixing characteristics discussed here, buoyancy reversal is typically discussed in the context of mixing between two air parcels, one with cloud droplets and the other one subsaturated and cloud-free. *Grabowski* [1993] shows that local buoyancy during mixing can differ significantly from the buoyancy of the homogenized parcel. Hence, concepts originating from two-parcel bulk mixing really do not apply at the cloud microscale. See also Figures 3 and 4 in *Malinowski et al.* [2008] and their discussion.

Results discussed in this paper suggest that highly idealized DNS (i.e., based on the first principles) with Lagrangian droplets can provide results relevant to entrainment-induced changes of DSDs observed in natural clouds. Arguably, the next step should involve inclusion of the physics that would make DNS even closer to natural clouds. In particular, one can envision incorporation of stratification effects that would lead to droplet growth and evaporation in response to the vertical motion. With ever increasing computational power, DNS simulations in domains large enough to make them relevant to natural clouds are only a matter of time. For instance, such DNS simulations are already conducted, applying idealized thermodynamics [e.g., *Abma et al.*, 2013; *Mellado et al.*, 2014; *de Lozar and Mellado*, 2015]. We plan on continuing model development along the lines outlined above and report the progress in future publications.

Appendix A: Details of DNS Model

The description of the Euler-Lagrangian model used in this study is given below. More details are given in *Kumar et al.* [2014].

A1. Eulerian

The Eulerian equations for the turbulent fields, namely the velocity field \mathbf{u} , the vapor mixing ratio field q_v , and the temperature field T , are given by

$$\nabla \cdot \mathbf{u} = 0, \quad (\text{A1})$$

$$\partial_t \mathbf{u} + (\mathbf{u} \cdot \nabla) \mathbf{u} = -\frac{1}{\rho_0} \nabla p + \nu \nabla^2 \mathbf{u} + B \mathbf{e}_z, \quad (\text{A2})$$

$$\partial_t T + \mathbf{u} \cdot \nabla T = \kappa \nabla^2 T + \frac{L}{c_p} C_d, \quad (\text{A3})$$

$$\partial_t q_v + \mathbf{u} \cdot \nabla q_v = D \nabla^2 q_v - C_d, \quad (\text{A4})$$

where $\rho_0 = 1.06 \text{ kg m}^{-3}$ is the air density; p is the pressure perturbation derived from the incompressibility assumption (A1); ν , κ , and D are air viscosity, air thermal conductivity, and diffusivity of water vapor in air, respectively; B is buoyancy; L and c_p are latent heat of condensation and air specific heat at constant pressure; C_d is condensation rate. The buoyancy B is defined as

$$B(\mathbf{x}, t) = g \left[\frac{T - T_0}{T_0} + \tilde{\epsilon} (q_v - q_{v0}) - q_l \right], \quad (\text{A5})$$

where $\tilde{\epsilon} = R_v/R_d - 1 \approx 0.608$. Here R_v is the vapor gas constant and R_d the dry air gas constant. The cloud water mixing ratio q_l and the condensation rate C_d in the Eulerian flow model are derived from the mass and the rate of change of mass of all droplets within a given gridbox of the model.

A2. Lagrangian

The cloud droplets are described by

$$\frac{d\mathbf{X}}{dt} = \mathbf{V}(\mathbf{X}, t), \quad (\text{A6})$$

$$\frac{d\mathbf{V}}{dt} = \frac{1}{\tau_p} [\mathbf{u}(\mathbf{X}, t) - \mathbf{V}(\mathbf{X}, t)] + \mathbf{g}, \quad (\text{A7})$$

$$r(\mathbf{X}, t) \frac{dr(\mathbf{X}, t)}{dt} = K S(\mathbf{X}, t), \quad (\text{A8})$$

where \mathbf{X} is the droplet position, \mathbf{V} is the droplet velocity, and r is the radius. We describe cloud water droplets as inertial point particles with a finite particle response time $\tau_p = 2\rho_l r^2 / (9\rho_0 \nu)$ that grow and evaporate by the diffusion of vapor. The vector $\mathbf{g} = (0, 0, -g)$ is the gravitational acceleration, and K is the coefficient in the droplet growth equation.

Acknowledgments

CAIPEEX airborne observational program is funded by Ministry of Earth Science, Government of India and executed by a team of scientists from IITM, Pune. Authors thank to Director, IITM for his encouragement and support to this work. Authors also acknowledge the support from HPCS, IITM for providing access to Aaditya supercomputing facility (<http://aadityahpc.tropmet.res.in/Aaditya/index.html>), for carrying out the simulation and using data storage. NCAR is supported by the U.S. National Science Foundation. WWG acknowledges IITM financial support and hospitality during his visits to IITM.

References

- Abma, D., T. Heus, and J.-P. Mellado (2013), Direct numerical simulations of evaporative cooling at the lateral boundary of shallow cumulus clouds, *J. Atmos. Sci.*, *70*, 2088–2102, doi:10.1175/JAS-D-12-0230.1.
- Andrejczuk, M., W. W. Grabowski, S. P. Malinowski, and P. K. Smolarkiewicz (2004), Numerical simulation of cloud-clear air interfacial mixing, *J. Atmos. Sci.*, *61*, 1726–1739.
- Andrejczuk, M., W. W. Grabowski, S. P. Malinowski, and P. K. Smolarkiewicz (2006), Numerical simulation of cloud-clear air interfacial mixing: Effects on cloud microphysics, *J. Atmos. Sci.*, *63*, 3204–3225.
- Andrejczuk, M., W. W. Grabowski, S. P. Malinowski, and P. K. Smolarkiewicz (2009), Numerical simulation of cloud-clear air interfacial mixing: Homogeneous versus inhomogeneous mixing, *J. Atmos. Sci.*, *66*, 2493–2500.
- Baker, M. B., and J. Latham (1979), The evolution of droplet spectra and the rate of production of embryonic raindrops in small cumulus clouds, *J. Atmos. Sci.*, *36*, 1612–1615.
- Baker, M. B., R. G. Corbin, and J. Latham (1980), The influence of entrainment on the evolution of cloud drop spectra: I. A model of inhomogeneous mixing, *Q. J. R. Meteorol. Soc.*, *106*, 581–598.
- Baker, M. B., R. E. Breidenthal, T. W. Choullarton, and J. Latham (1984), The effects of turbulent mixing in clouds, *J. Atmos. Sci.*, *41*, 299–304.
- Bera, S., G. Pandithurai, and T. V. Prabha (2016a), Entrainment and droplet spectral characteristics in convective clouds during transition to monsoon, *Atmos. Sci. Lett.*, *17*, 286–293, doi:10.1002/asl.657.
- Bera, S., T. V. Prabha, and W. W. Grabowski (2016b), Observations of monsoon convective cloud microphysics over India and role of entrainment-mixing, *J. Geophys. Res. Atmos.*, *121*, 9767–9788, doi:10.1002/2016JD025133.
- Brenguier, J. L., and W. W. Grabowski (1993), Cumulus entrainment and cloud droplet spectra: A numerical model within a two-dimensional dynamical framework, *J. Atmos. Sci.*, *50*, 120–136.
- Brenguier, J. L., H. Pawlowska, L. SchÄijler, R. Preusker, J. Fischer, and Y. Fouquart (2000), Radiative properties of boundary layer clouds: Droplet effective radius versus number concentration, *J. Atmos. Sci.*, *57*, 803–821.
- Burnet, F., and J. L. Brenguier (2007), Observational study of the entrainment-mixing process in warm convective clouds, *J. Atmos. Sci.*, *64*, 1995–2011.
- Carpenter, R. L., Jr., K. Kelvin, and A. M. Blyth (1998a), Entrainment and detrainment in numerically simulated cumulus congestus clouds. Part I: General Results, *J. Atmos. Sci.*, *55*(23), 3417–3432.

- Carpenter, R. L., Jr., K. Kelvin, and A. M. Blyth (1998b), Entrainment and detrainment in numerically simulated cumulus congestus clouds. Part II: General Results, *J. Atmos. Sci.*, *55*(23), 3433–3439.
- Carpenter, R. L., Jr., K. Kelvin, and A. M. Blyth (1998c), Entrainment and detrainment in numerically simulated cumulus congestus clouds. Part III: Parcel Analysis, *J. Atmos. Sci.*, *55*(23), 3440–3455.
- Cooper W. A. (1989), Effects of variable droplet growth histories on droplet size distributions. Part I: Theory, *J. Atmos. Sci.*, *46*, 1301–1311.
- Cooper, W. A., S. G. Lasher-Trapp, and A. M. Blyth (2013), The influence of entrainment and mixing on the initial formation of rain in a warm cumulus cloud, *J. Atmos. Sci.*, *70*(6), 1727–1743.
- de Lozar, A., and J.-P. Mellado (2015), Mixing driven by radiative and evaporative cooling at the stratocumulus top, *J. Atmos. Sci.*, *72*, 4681–4700, doi:10.1175/JAS-D-15-0087.1.
- Devenish, B. J., et al. (2012), Droplet growth in warm turbulent clouds, *Q. J. R. Meteorol. Soc.*, *138*, 1401–1429.
- Gerber, H., G. Frick, J. Jensen, and J. Hudson (2008), Entrainment, mixing, and microphysics in trade-wind cumulus, *J. Meteorol. Soc. Jpn.*, *86A*, 87–106.
- Grabowski, W. W. (1993), Cumulus entrainment, fine-scale mixing, and buoyancy reversal, *Q. J. R. Meteorol. Soc.*, *119*, 935–956, doi:10.1002/qj.49711951305.
- Grabowski, W. W., and T. L. Clark (1991), Cloud-environment interface instability: Rising thermal calculations in two spatial dimensions, *J. Atmos. Sci.*, *48*(4), 527–546.
- Grabowski, W. W., and T. L. Clark (1993a), Cloud-environment interface instability: Part II: Extension to three spatial dimensions, *J. Atmos. Sci.*, *50*(4), 555–573.
- Grabowski, W. W., and T. L. Clark (1993b), Cloud-environment interface instability: Part III: Direct influence of environmental shear, *J. Atmos. Sci.*, *50*(23), 3821–3828.
- Grabowski, W. W., and P. Vaillancourt (1999), Comments on Preferential concentration of cloud droplets by turbulence: Effects on the early evolution of cumulus cloud droplet spectra, *J. Atmos. Sci.*, *56*, 1433–1436.
- Herring, J. R., and R. M. Kerr (1993), Development of enstrophy and spectra in numerical turbulence, *Phys. Fluids A*, *5*, 2792–2798.
- Hoffman, F., H. Siebert, J. Schumacher, T. Riechelmann, J. Katzwinkel, B. Kumar, P. G. A.ützfried, and S. Raasch (2014), Entrainment and mixing at the interface of shallow cumulus clouds: Results from a combination of observations and simulation, *Meteorol. Z.*, *23*(4), 349–368, doi:10.1127/0941-2948/2014/0597.
- Jarecka, D., H. Pawlowska, W. W. Grabowski, and A. A. Wyszogrodzki (2013a), Modeling microphysical effects of entrainment in clouds observed during EUCAARI-IMPACT field campaign, *Atmos. Chem. Phys. Discuss.*, *13*, 1489–1526, doi:10.5194/acpd-13-1489-2013.
- Jarecka, D., W. W. Grabowski, H. Morrison, and H. Pawlowska (2013b), Homogeneity of subgrid-scale turbulent mixing in large eddy simulation of shallow convection, *J. Atmos. Sci.*, *70*, 2751–2767.
- Jensen, J. B., and M. B. Baker (1989), A simple model of droplet spectral evolution during turbulent mixing, *J. Atmos. Sci.*, *46*(18), 2812–2829.
- Khain, A., T. V. Prabha, N. Benmoshe, G. Pandithurai, and M. Ovchinnikov (2013), The mechanism of first raindrops formation in deep convective clouds, *J. Geophys. Res.*, *118*, 9123–9140, doi:10.1002/jgrd.50641.
- Kumar, B., F. Janetzko, J. Schumacher, and R. A. Shaw (2012), Extreme responses of a coupled scalar-particle system during turbulent mixing, *New J. Phys.*, *14*, 115020, doi:10.1088/1367-2630/14/11/115020.
- Kumar, B., J. Schumacher, and R. A. Shaw (2013), Cloud microphysical effects of turbulent mixing and entrainment, *Theor. Comput. Fluid Dyn.*, *27*(3), 361–376, doi:10.1007/s00162-012-0272-z.
- Kumar, B., J. Schumacher, and R. A. Shaw (2014), Lagrangian mixing dynamics at the cloudy-clear air interface, *J. Atmos. Sci.*, *71*(7), 2564–2580, doi:10.1175/JAS-D-13-0294.1.
- Lasher-Trapp, S. G., W. A. Cooper, and A. M. Blyth (2005), Broadening of droplet size distributions from entrainment and mixing in a cumulus cloud, *Q. J. R. Meteorol. Soc.*, *131*, 195–220.
- Lehmann, K., H. Siebert, and R. A. Shaw (2009), Homogeneous and inhomogeneous mixing in cumulus clouds: Dependence on local turbulence structure, *J. Atmos. Sci.*, *66*, 3641–3659.
- Liu, Y., P. H. Daum, and S. S. Yum (2006), Analytical expression for the relative dispersion of the cloud droplet size distribution, *Geophys. Res. Lett.*, *33*, L02810, doi:10.1029/2005GL024052.
- Malinowski, S. P., M. Andrejczuk, W. W. Grabowski, P. Korczyk, T. A. Kowalewski, and P. K. Smolarkiewicz (2008), Laboratory and modeling studies of cloud-clear air interfacial mixing: Anisotropy of small-scale turbulence due to evaporative cooling, *New J. Phys.*, *10*, 15 pp., doi:10.1088/1367-2630/10/7/075020.
- Mellado, J.-P., B. Stevens, and H. Schmidt (2014), Wind shear and buoyancy reversal at the stratocumulus top, *J. Atmos. Sci.*, *71*, 1040–1057, doi:10.1175/JAS-D-13-0189.1.
- Prabha, T. V., A. Khain, R. S. Maheshkumar, G. Pandithurai, J. R. Kulkarni, M. Konwar, and B. N. Goswami (2011), Microphysics of pre-monsoon and monsoon clouds, *J. Atmos. Sci.*, *68*, 1882–1901, doi:10.1175/2011JAS3707.1.
- Prabha, T. V., S. Patade, G. Pandithurai, A. Khain, D. Axisa, P. P. Kumar, R. S. Maheshkumar, J. R. Kulkarni, and B. N. Goswami (2012), Spectral width of premonsoon and monsoon clouds over Indo-Gangetic valley, *J. Geophys. Res.*, *117*, D20205, doi:10.1029/2011JD016837.
- Shaw, R. A. (2003), Particle-turbulence interactions in atmospheric clouds, *Annu. Rev. Fluid Mech.*, *35*, 183–227.
- Shaw, R. A., W. C. Reade, L. R. Collins, and J. Verlinde (1998), Preferential concentration of cloud droplets by turbulence: Effects on the early evolution of cumulus cloud droplet spectra, *J. Atmos. Sci.*, *55*, 1965–1976.
- Slawinska, J., W. W. Grabowski, H. Pawlowska, and H. Morrison (2012), Droplet activation and mixing in large-eddy simulation of a shallow cumulus field, *J. Atmos. Sci.*, *69*, 444–462.
- Stevens, B., et al. (2005), Evaluation of large-eddy simulations via observations of nocturnal marine stratocumulus, *Mon. Weather Rev.*, *133*, 1443–1462.
- Tölle, M. H., and S. K. Krueger (2014), Effects of entrainment and mixing on droplet size distributions in warm cumulus clouds, *J. Adv. Model. Earth Syst.*, *6*, 281–299, doi:10.1002/2012MS000209.
- Telford, J. W., and S. K. Chai (1980), A new aspect of condensation theory, *PageOph*, *118*, 720–742.
- Vaillancourt, P., M. K. Yau, and W. W. Grabowski (2001), Microscopic approach to cloud droplet growth by condensation. Part I: Model description and results without turbulence, *J. Atmos. Sci.*, *58*, 1945–1964.
- VanZanten, M. C., et al. (2011), Controls on precipitation and cloudiness in simulations of trade-wind cumulus as observed during RICO, *J. Adv. Model. Earth Syst.*, *3*, M06001, doi:10.1029/2011MS000056.
- Yum, S. S., J. Wang, Y. Liu, G. Senum, S. Springston, R. McGraw, and J. M. Yeom (2015), Cloud microphysical relationships and their implication on entrainment and mixing mechanism for the stratocumulus clouds measured during the VOCALS project, *J. Geophys. Res.*, *22*, 5047–5069, doi:10.1002/2014JD022802.
- Zhao, M., and P. H. Austin (2005a), Life cycle of numerically simulated shallow cumulus clouds. Part I: Transport, *J. Atmos. Sci.*, *62*(5), 1269–1290.
- Zhao, M., and P. H. Austin (2005b), Life cycle of numerically simulated shallow cumulus clouds. Part II: Mixing Dynamics, *J. Atmos. Sci.*, *62*(5), 1291–1310.